Effect of the preparation techniques of photopolymerizable ceramic slurry and printing parameters on the accuracy of 3D printed lattice structures

Kova¿ev, Nikolina; Li, Sheng; Essa, Khamis

DOI:
10.1016/j.jeurceramsoc.2021.08.052

Document Version
Peer reviewed version

Citation for published version (Harvard):
Kova¿ev, N, Li, S & Essa, K 2021, 'Effect of the preparation techniques of photopolymerizable ceramic slurry and printing parameters on the accuracy of 3D printed lattice structures', *Journal of the European Ceramic Society*, vol. 41, no. 15, pp. 7734-7743. https://doi.org/10.1016/j.jeurceramsoc.2021.08.052

Effect of the preparation techniques of photopolymerizable ceramic slurry and printing parameters on the accuracy of 3D printed lattice structures

Nikolina Kovacev*, Sheng Li, Khamis Essa**

School of Mechanical Engineering, University of Birmingham, Edgbaston, B15 2TT, United Kingdom

Abstract

Digital Light Processing (DLP) technology demonstrates the potential for manufacturing parts with complex structures for various engineering applications. The purpose of this study is to evaluate Al_2O_3 ceramic slurry preparation techniques, establish optimal processing window and assess the manufacturability and dimensional accuracy of lattice structures with CAD strut diameters of up to 500 µm. Two preparation techniques of the ceramic slurry were investigated. The slurry with the pre-treated powder showed appropriate rheological and photopolymerization behaviour. Full factorial Design of Experiments (DOE) was conducted to generate an experimental plan and assess the influence of the printing parameters on the dimensional accuracy. Analysis of Variance (ANOVA) revealed the exposure time, the exposure power, and the interaction effect of both had a significant influence on the dimensional accuracy of lattice strut diameters. The excess cure width was found to be dependent on the feature size, the energy dose and the layer thickness.

Keywords: additive manufacturing, DLP, ceramic slurry, lattice, DOE

* Corresponding author.
** Corresponding author.
E-mail address: nxk889@bham.ac.uk (N. Kovacev).
k.e.a.essa@bham.ac.uk (K.Essa).

1. Introduction

There is a rapidly growing demand for lattice structures in the industry for various applications ranging from porous bio ceramics in regenerative medicine, reducing the weight of parts for industrial applications, for optical applications, as well as monolithic supports for catalytic applications [1–8]. However, their manufacturing is impossible via well-established conventional methods. A promising alternative to conventional manufacturing is additive manufacturing. Additive manufacturing (AM) is a process of three-dimensional object manufacturing via the addition of individual layers according to a sliced Computer-Aided Design (CAD) model. Considering the materials processed, plastics and metal AM are currently leading on the market, whereas ceramic AM has been gaining lots of interest recently [9, 10]. Ceramic AM is generally divided into two categories: indirect and direct. Direct AM processes include selective laser sintering/melting (SLS/SLM), direct inkjet printing (DIP) and robocasting, amongst others. The majority of the ceramic AM processes include indirect technologies [11]. These are, to name a few, Laminated Object Manufacturing (LOM), Indirect Selective Laser Sintering (SLS) and Stereolithography (SLA). Stereolithography (SLA) dates to the early 1980s and is one of the widely used forms of ceramic additive manufacturing. Digital Light Processing (DLP) based on mask-image projection and laser-based Stereolithography (SLA) based on spot scanning both work on the principle of the photopolymerization of a ceramic slurry. The advantage of DLP technology is a faster realization of an object as the projected image hardens a layer of slurry at a time [12]. A critical aspect of the AM is to achieve dimensional accuracy and repeatability of the manufactured parts [13]. Detailed studies on the influence of the printing parameters on the part dimensions are generally found for metal AM. Metal lattice structures with fine strut diameters were fabricated in the past by Laser Powder Bed Fusion [14] and Selective Laser Melting [15]. The investigation of the laser power and scanning speed on the dimensional accuracy of the strut diameter of a diamond lattice cell showed the increase of the strut diameter with the increase of the laser power [16]. Similarly, Qiu et al. [17] found that the deviations of the experimental strut diameter from the designed value were increasing with the increase of the laser power [17]. The influence of the printing parameters on the dimensional accuracy for ceramic stereolithography based processes is not widely investigated. Generally, the studies on accuracy include bulk structures, walls, or gaps. Fu et al. [18] studied the influence of the laser power on the dimensional accuracy of SLA of bulk products, concluding that the length and width increased with the increase of the laser power due to the increase of the light scattering [18]. A study of printability and lateral accuracy of holes and walls with lithography-based AM showed holes down to 200 μm could be fabricated, but those smaller than 500 μm would have a large deviation from the CAD design [19]. Similarly, the dimensional accuracy of designed hexahedral cavities in a lattice structure manufactured by lithography-based technology was evaluated. Manufactured cavities were 15 to 30% smaller as compared to theoretical values [20]. Schhauer et al. [21] reported successful manufacturing of a honeycomb structure with a wall thickness of 100 μm. However, the experiments revealed that the holes with diameters of less than 200 μm were clogged [21]. In another study, the printing parameters were experimentally varied in manufacturing of a gear geometry via LCM and it was found the horizontal resolution increased with the decrease of the exposure energy. The diameter of the hole presented higher dimensional difference for all sets of printing parameters [22]. Manufacturing parts that contain small

features, such as lattice structure is challenging, due to their small features. Although complex Al_2O_3 and TiO_2 lattice structures with 170 µm and 200 µm strut diameter were manufactured in past, the debinding and sintering processes needed optimization and strict control to obtain samples without cracks since low solid loadings caused high shrinkage up to 70% during thermal postprocessing [23, 24].

The slurries suitable for ceramic AM contain ceramic filler mixed in with binder, photoinitiator and other additives. For ceramic additive manufacturing ceramic particles such as alumina (Al_2O_3), pure zirconia (ZrO_2), zirconia stabilized with yittria, silicon dioxide (SiO_2), hydroxyapatite, cordierite, and others can be used as the ceramic filler [25–29]. The dimensional inaccuracy in ceramic-based stereolithography is a consequence of scattering caused by the addition of the ceramic particles to the UV resin [7, 30]. High refractive index difference between the ceramic particle and photopolymerizable resin results in a reduction of cure depth and distortion of the resolution [30, 31]. The working curve of the ceramic slurry describes the thickness to which a slurry cures as a function of the light dose for a given light source. Polymerization depth in vertical direction C_d, can be expressed empirically with Jacob's equation:

$$C_d = D_p \ln\left(\frac{E}{E_c}\right) \qquad \text{Eq. 1}$$

where D_p is the depth of penetration, E is the exposure energy density on the slurry surface, and E_c is the critical exposure energy density of the slurry [32]. The critical exposure energy density presents the minimum energy density required for photopolymerization of the slurry [33]. The depth of penetration presents the distance at which the light intensity is reduced by e^{-1} [34]. E_c and D_p are solely parameters of the resin that do not depend on the exposure parameters. Bennet [35] performed experiments with various light intensities and proved that D_p and E_c for each power density vary by about 10% and 3%, respectively. This minor variation was attributed to the errors in the measurements of the cure depths and power densities [35]. Gentry and Halloran [30] proposed a quasi-Beer-Lambert relationship between the excess cure width (C_w) and the energy dose:

$$C_w = D_w \ln\left(\frac{E}{E_w}\right) \qquad \text{Eq. 2}$$

where D_w is the width sensitivity and E_w is the width critical energy dose. Broadening parameters D_w and E_w are affected by the scattering of the light, the absorption and the critical energy dose of the resin [30]. In their work, the semilogarithmic dependence of excess line width on energy dose was proven for various ceramic suspension. They introduced broadening depth (B_d) which is the depth of the cure at the onset of broadening:

$$B_d = D_p \ln\left(\frac{E_w}{E_c}\right) \qquad \text{Eq. 3}$$

Rudraraju [36] demonstrated that with DMD projection the broadening behaviour depends upon the feature size, the energy dose and the cure depth by curing 2D squares with the size of 25-900 pixels [36]. The reported behaviour is studied only for experiments where a single-layer is cured; hence it is necessary to determine whether this is the case when a 3D object is manufactured as subsequent layer curing can affect print-through to the previous layer.

Dissimilar routes of ceramic suspension preparation are present in the literature. The ceramic powder can be either used as-received [32, 37–40] or the surface of the ceramic particle can be pre-treated with a dispersant prior to the addition to the photopolymerizable resin [34, 41, 42]. Clear indication of the best method of preparation and evidence of the photopolymerization behaviour and rheology is lacking. An important factor in the development of the ceramic slurry is to achieve a solid loading of over 40 vol% [25, 28, 32]. On the one hand, high solid loading is desirable as it improves the mechanical properties and reduces sintering shrinkage. On the other hand, the introduction of the hydrophilic ceramic particles into the hydrophobic resin drastically increases the viscosity. To achieve a high solid loading and good dispersion of the ceramic particles in the resin, it is required to add a dispersant to provide steric barriers between ceramic particles that compensates van der Waals attractive forces between them and prevents collision of the particles caused by Brownian motion [32]. The recommended rheology of the suspension for Admaflex technology is a Non-Newtonian behaviour with shear thinning and a dynamic viscosity below 10 Pa·s for shear rates of 10 to 300 s^{-1} [43].

In summary, fine-tuning the process parameters is important for precise part manufacturing. Developing ceramic slurry with high solid loading, low viscosity and good resolution is the key issue for ceramic stereolithography based additive manufacturing. The accuracy of parts manufactured by DLP technology is a complex interaction between process parameters, printer resolution and formulation of the photopolymerizable slurry. Although there have been various studies focusing on the effects of printing parameters on the performance of fabricated parts, systematic investigation on the effects of slurry preparation and printing parameters on the dimensional accuracy for DLP additive manufacturing of lattice structures with small features (<500 μm) is required. Broadening of various feature sizes in 3D object at different layer thicknesses and energy doses must be studied to assess the broadening behaviour. The aim of this study is to evaluate ceramic slurry preparation techniques and to establish optimal printing parameters. Two distinct procedures of the addition of the ceramic powder in the photoreactive resin were considered for the preparation of low viscosity, high reactive alumina slurry. The effect of the pre-treatment of the ceramic particles compared to as-received powder was studied in terms of rheology and photopolymerization. To address the gaps in the literature, the effort to understand the effect of the layer thickness, exposure power and exposure time on the dimensional accuracy of lattice strut diameters are investigated by adopting statistical approaches by means of a full-factorial design of experiment (DOE) and Analysis of Variance (ANOVA). The determination of the optimum process parameters is conducted based on the evaluation of the printing dimensional accuracy compared with CAD models.

2. Methodology

2.1. Ceramic slurry preparation and characterisation

The resin consisted of a mono-functional, di-functional and tetra-functional monomer and plasticizer in the appropriate proportions [43]. Phosphoric ester salt of a high molecular weight copolymer with pigment-affinic groups was selected as the dispersant (BYK-Chemie GmbH, Wesel, Germany). Diphenyl (2,4,6-trimethylbenzoyl) phosphine oxide (Sigma Aldrich, Gillingham, UK) was used as the initiator of the polymerization reaction. Commercially available alumina oxide powder (A16 SG, Almatis GmbH,

Ludwigshafen, Germany) was used as the ceramic filler. **Table 1** contains the particle size distribution of the as-received (AR) powder and the pre-treated (PT) alumina powder.

Table 1 Ceramic powders used in the photopolymerizable ceramic suspensions

Material	**d_{10}, µm**	**d_{50}, µm**	**d_{90}, µm**
Al_2O_3- As-Received (AR)	0.22	0.80	4.90
Al_2O_3- Pre-treated (PT)	0.23	0.80	2.31

The particle size distribution of the ceramic powder was evaluated with Sympatec Helos (Sympatec GmbH, Clausthal-Zellerfeld, Germany) using R1 lens. The morphology of the powder was examined using SEM (Jeol JCM 600, Tokio, Japan). **Fig. 1** shows **a)** the particle size distribution curves of the powders and SEM images of **b)** AR powder and **c)** PT powder. The AR powder consists of large, spherical, aggregated particles (**Fig. 1 b)**); after milling the agglomerates appeared less spherical, and some large flaked particles can be observed from **Fig. 1 c)**.

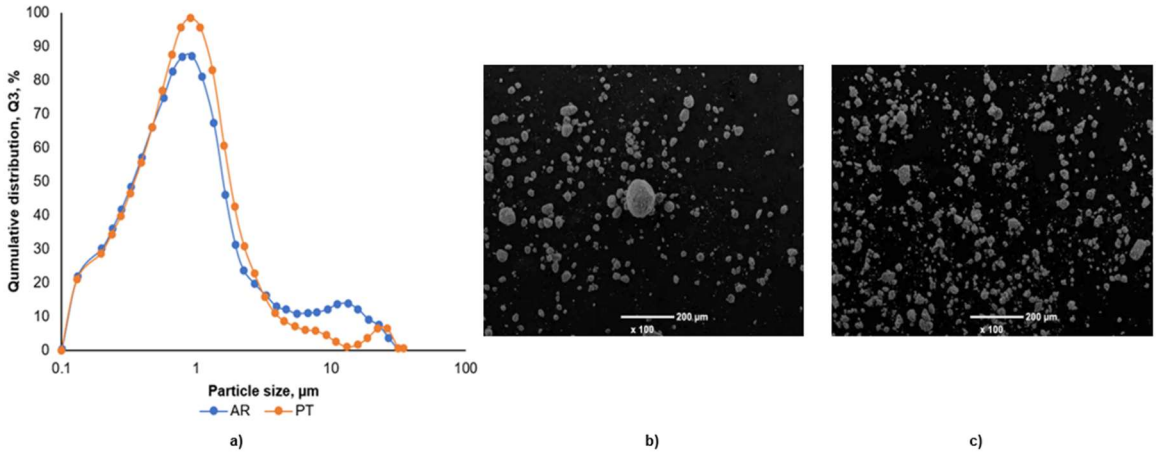

Fig. 1. a) Particle size distribution curves, b) SEM of the as-received powder and c) SEM of the PT powder

The ceramic slurry preparation procedures were adapted from the literature [43]. The first procedure included combining resin components with an overhead mixer at room temperature for 30 minutes, followed by addition of 2 wt% of dispersant. The mixture was stirred for an additional hour. The AR powder was added in small increments until the solid loading of 57 vol% was reached. Finally, a small amount of photoinitiator was added into the mixture together with zirconia oxide grinding media of the same mass weight as the powder and the slurry was placed on the roller for 24 h. In the second procedure, the AR ceramic powder was combined with ethanol and 2 wt% of the dispersant followed by planetary ball milling with 1 mm zirconia grinding media at 400 rpm for 2 hours. The mixture was first air-dried for 24 h and then dried in the oven for 12 h at 110 °C to allow solvent decomposition. The PT dry powder was sieved through a mesh of 250 µm and added into the resin until the solid loading of 57 vol% was achieved. This was followed by addition of the photoinitiator and zirconia oxide grinding media of the same mass weight as the powder. Lastly, the slurry was placed on the roller for 24 h.

Rheological behaviour of the ceramic suspensions was tested on AR 500 (TA Instruments, New Castle DE, USA) with a 20 mm gold on rhodium plate varying the shear rate from 0.1 to 300 s^{-1} at a constant temperature of 20.6 °C. The refractive index of the resin was measured using a digital pocket refractometer at T=18.5 °C (ATAGO CO., LTD., Tokyo, Japan). A single-layer curing method was used for measurement of the cure depth at various exposure energies to determine the critical exposure energy and depth of penetration. Prior to the measurement, the prepared slurries were treated in a vacuum degasser for 10 minutes to remove the air bubbles and reduce the inhibition polymerization. An image of a checkboard pattern was projected to a layer of photopolymerizable resin. Cured layers were peeled off the foil and the thickness of the cured material was determined with a handheld micrometer (Mitutoyo Digimatic Micrometer, MDC-25PX, Kawasaki, Japan). Three consequent measurements were made, and the average cure depth was recorded.

2.2. Design of the lattice structures

The lattice structures designed for this study were based on a unit cell of a diamond lattice elongated in the z-direction. The dimensions of the repeating unit cell were 1.25 mm (x) by 1.25 mm (y) by 2.5 mm (z). The strut diameter was varied from 100 µm to 500 µm to study the manufacturability and the effect of the processing parameters on the dimensional accuracy. The generated CAD diagram is shown in **Fig. 2**.

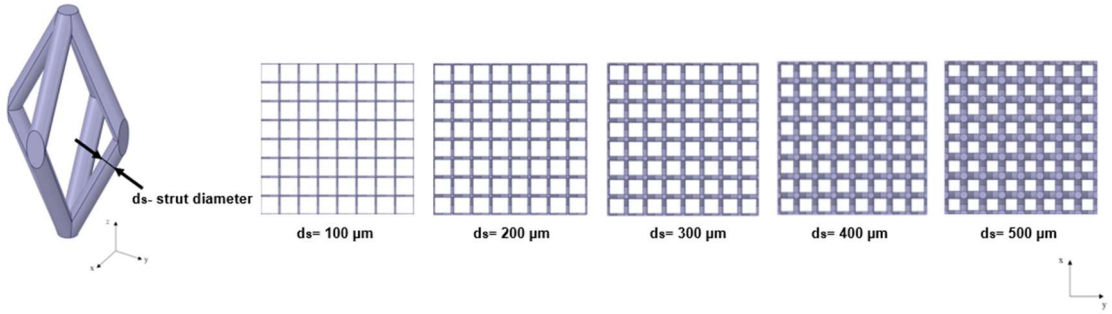

Fig. 2. CAD design of lattices with varying strut diameter

2.3. Experimental design

Full factorial Design of Experiments (DOE) was conducted to generate an experimental plan and assess the influence of the printing parameters on the dimensional accuracy of lattices with various CAD strut diameters. The analysis of Variance (ANOVA) was used to identify the significant printing parameters and interactions on the process outputs [13]. The factors selected for the experiments were exposure time (ET), exposure power (EP) and sliced layer thickness (LT). Three levels were selected for the exposure time and the exposure power and two levels for layer thickness (**Table 2**). The exposure power is expressed as a certain percentage of the maximum light intensity of the DLP light source, yielding irradiance of 6.72 mW/cm^2 for 10%, 14 mW/cm^2 for 20% and 20.79 mW/cm^2 for 30%. Sliced layer thickness is the thickness of each individual slice of the model. The exposure time is the duration where the resin is exposed under a light source for each layer. Layer curing times of only 1.5–3 seconds were required due to the high reactivity of the resin.

Table 2 Factors, levels, and their corresponding values for the experimental test

Factors	Levels		
	L1	**L2**	**L3**
Exposure time (ET), s	1.5	2	3
Exposure power (EP), mW/cm^2	6.72	14	20.79
Sliced layer thickness (LT), µm	10	25	-

Table 3 presents the experimental matrix for the full factorial experiment. The total number of conducted experiments was 18 for each lattice sample. To study the statistical significance of factor effects on each response, the analysis of variance (ANOVA) using Minitab 19 statistical software was performed.

Table 3 Experimental matrix

Run	ET, s	EP, mW/cm^2	LT, µm
1	1.5	6.72	10
2	1.5	14	10
3	1.5	20.79	10
4	2.0	6.72	10
5	2.0	14	10
6	2.0	20.79	10
7	3.0	6.72	10
8	3.0	14	10
9	3.0	20.79	10
10	1.5	6.72	25
11	1.5	14	25
12	1.5	20.79	25
13	2.0	6.72	25
14	2.0	14	25
15	2.0	20.79	25
16	3.0	6.72	25
17	3.0	14	25
18	3.0	20.79	25

The diameters of the struts of the green parts were determined from images taken by Alicona InfiniteFocusG5 plus (Bruker Alicona, Leicestershire, UK) optical microscope using a 5× objective. The strut diameter measurements were taken at the edges of the samples and an average was calculated from the total of 16 measurements for each of the 18 conditions in **Table 3.** The dimensional effectiveness of the printing process was assessed through printing accuracy represented by the calculated linear dimensional

change of the strut diameter of as-printed green parts, compared with those of the original CAD model presented by:

$$D(i) = \frac{d_{s,CAD} - d_{si}}{d_{s,CAD}} \times 100\ \% \qquad \text{Eq. 4}$$

Where $D(i)$ is deviation, $d_{s,CAD}$ is the CAD strut diameter and d_{si} strut diameter of the as-printed green samples.

2.4. Additive manufacturing

The printing experiments were conducted on the Admaflex 130 (Admatec Europe BV, Alkmaar, The Netherlands) working with a light source of λ =405 nm and x,y resolution of 40 µm. The technology is based on Digital Light Processing with a DMD chip that comprises of thousands of mirrors that rotate according to pixels to project the image. The Admaflex 130 is equipped with a rotating foil system that transports the slurry on the foil from the reservoir to the manufacturing zone and to the pump where the excess slurry is pumped back to the reservoir. Photopolymerisable light-sensitive slurry is exposed to light which subsequently cures the whole layer. The process of curing layer by layer is repeated until the final three-dimensional green body is built. The printed parts were cleaned by using dibasic ester (Sigma Aldrich, Gillingham, UK) and compressed air. **Fig. 3.** shows the lattice samples produced on Admaflex 130 machine.

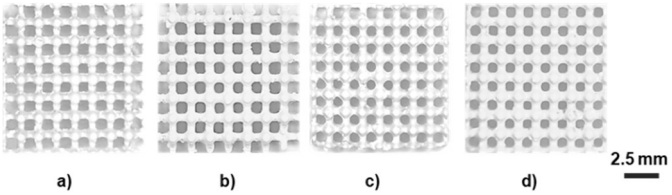

Fig. 3. Lattice samples produced on Admaflex 130

3. Results and discussion

3.1. Rheology of the ceramic slurry

The rheological behaviour of the prepared slurries expressed by viscosity curves as a function of shear rate is presented in **Fig. 4.** For comparison purpose, the rheological behaviour of the blank resin was plotted as well. The addition of the powder into the resin mixture highly increased the viscosity. The addition of the AR Al_2O_3 powder causes shear thickening at shear rates higher than 100 s^{-1}. The lower flowability of the AR Al_2O_3 slurry can be attributed to the agglomeration of the fine particles [29, 40]. In contrast, the shear-thinning behaviour (i.e. decreasing dynamic viscosity at higher shear rates) is shown by the suspension with the PT powder. With the pre-treatment of the powder by ball-milling and the dispersant, the level of agglomeration was reduced. The pre-treatment of the Al_2O_3 powder causes the adsorption of the dispersant on the particle surface resulting in more efficient dispersion of the ceramic particles in the resin. The viscosity of the prepared slurry with the pre-treated Al_2O_3 powder is lower than that of limit value for the Admaflex technology and considerably lower than that of the slurry with AR powder.

The critical exposure energy and depth of penetration were determined by performing a linear regression on the experimental C_d values plotted as a function of $\ln(E)$ as seen in **Fig. 5**. Both slurries had high cure

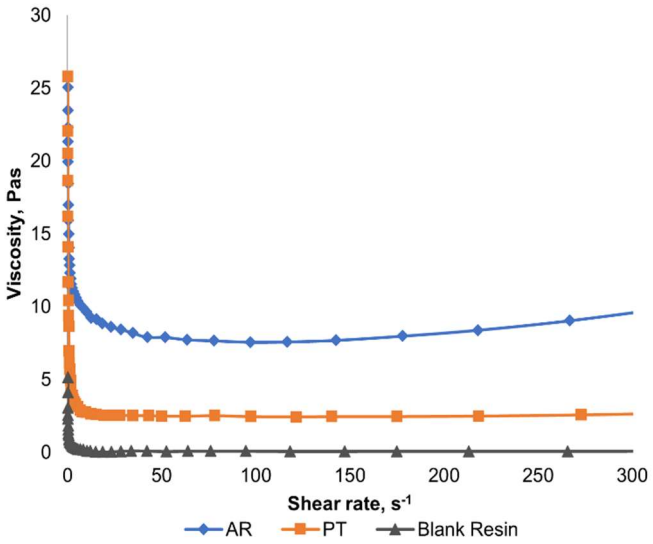

Fig. 4. Rheology of the ceramic slurries and the blank resin

depths at all energy densities. This can be contributed to the high reactivity of the resin. Equally, it is interesting to note the difference between the cure depths for the AR and PT powders.

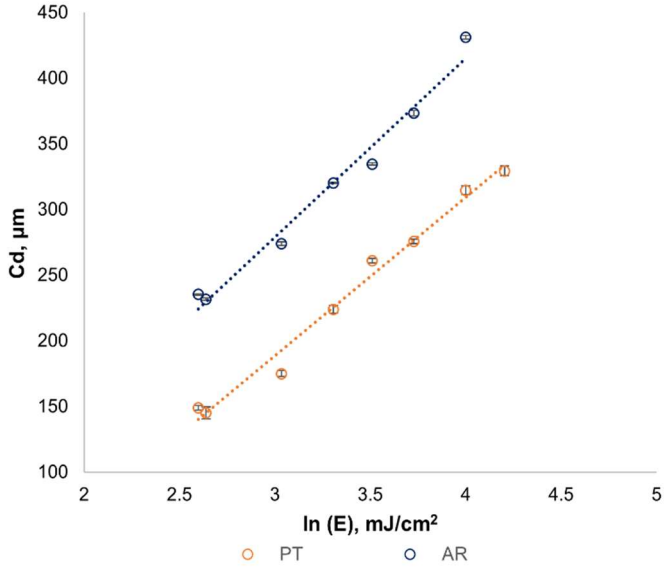

Fig. 5. The relation of the cure depth and the exposure energy density

The critical energy of the slurry with PT powder increased as seen in **Table 4**.

Table 4 The values of E_c and D_p

Suspension	E_c, mJ/cm^2	D_p, µm
w/AR Al_2O_3	5.47	136.04
w/PT Al_2O_3	9.03	120.74

This demonstrates how critical energy is altered by deagglomeration of the powder. The critical energy could similarly be increased by adding the appropriate inhibitors or absorbers into the suspension. However, those decrease the cure depth necessary for a stable part build up [44]. Depth of penetration has a significant impact on the polymerization width at the surface of a layer of the slurry. By pre-treatment of the powder, the D_p was decreased by 11 %. Lower D_p value allows better control of the lateral definition [45]. Suspensions prepared with the AR powder had greater C_d compared with suspensions prepared with PT ceramic particles, owing to the higher degree of scattering. Moreover, it was observed that the strong scattering effect caused by large agglomerates in AR powder results in poor spatial resolution. The ceramic slurry with PT powder showed better rheological and curing properties and is selected for further investigation.

3.2. Effect of the process parameters on the geometrical accuracy

The results of the DOE presented in **Table 3** are shown graphically in **Fig. 6**. Deviation from the CAD strut diameter was calculated based on Equation 4 (for layer thickness 10 and 25 µm) and used to represent the printing accuracy. The deviation from the CAD strut diameters is presented for each combination of the exposure time and the exposure power. Note that $d_{s,CAD}$ represents the strut diameter in the designed CAD model. From **Fig. 6 a)** and **b)** it can be seen that at constant exposure power, the increase of the exposure time, i.e. energy density, increases the deviation for each of the conditions. Furthermore, with the increase of the strut diameter, at constant exposure power and exposure time, the deviation is higher for larger strut dimensions. The actual strut diameters of fully dense samples were not measured; hence the fully dense samples represent 100% deviation in **Fig. 6**. The deviations for the conditions that resulted in a non-continuous build are not presented in the graph. For instance, lattices with designed CAD strut diameter of 100 µm were not mechanically stable during the manufacturing process and the complete failure of the part was observed in the initial layers; hence the deviations for the aforementioned are not shown in the graph. All successfully manufactured samples showed a positive deviation compared to the designed CAD strut diameter which is a consequence of light scattering effects caused by the different refractive indices of the resin and ceramic powder [19, 39, 46]. The results are in line with the findings in the literature for ceramic

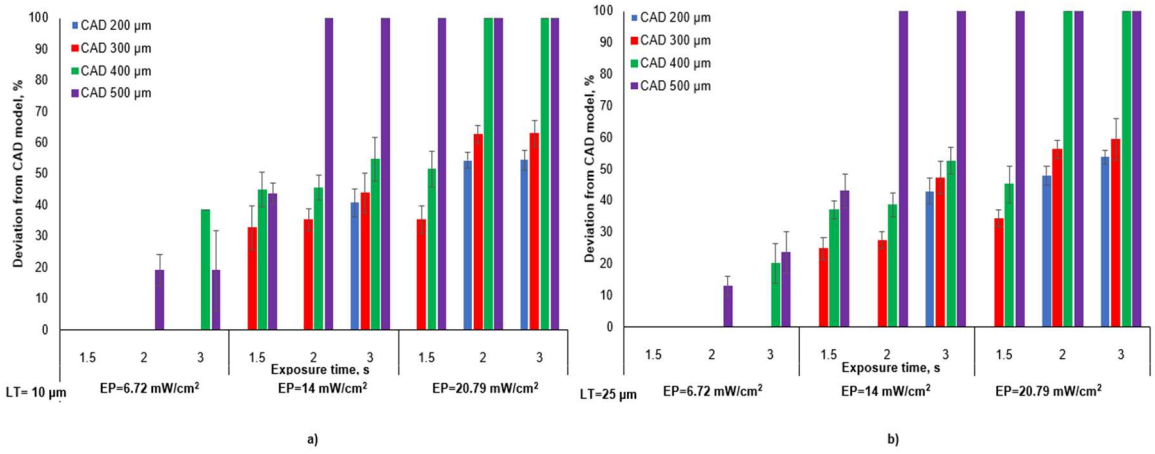

Fig. 6. Results of the DOE in terms of deviation from the CAD strut diameter model for a) LT= 10 µm and b) LT=25 µm

stereolithography processes which revealed that dimensions of the fabricated objects were higher than their designed values with the increase of energy density and exposed area [19, 39, 46].

ANOVA has been used to determine which parameters have the most influence on the printing accuracy of lattices with the designed CAD d_s of 200 µm to 500 µm. The layer thickness, the exposure time, the exposure power and their interaction are the source factors. The P-values for factors and their interactions are shown in **Table 5**. Based on a 95% confidence level, factors and interactions with P-value equal to or less than 0.05 are significant process parameters. Therefore, it can be concluded that the exposure time, the exposure power and their interaction are the most significant process parameters. The layer thickness is not considered as a significant parameter which was also observed in the literature [19].

Table 5 P-values for factors and their interactions

Source	**P-Values**			
	$d_{s,\,CAD}$= 200 µm	**$d_{s,\,CAD}$= 300 µm**	**$d_{s,\,CAD}$= 400 µm**	**$d_{s,\,CAD}$= 500 µm**
LT	0.455	0.131	0.148	0.837
ET	0.000	0.002	0.006	0.004
EP	0.000	0.000	0.001	0.000
LT*ET	0.337	0.444	0.787	0.449
LT*EP	0.252	0.473	0.798	0.981
ET*EP	0.000	0.009	0.001	0.000

Main effects and interaction plots assist in finding the optimal level of significant factors. Effect of significant process parameters and interactions are illustrated in **Fig. 7** and **Fig. 8**, respectively. The main effects demonstrate the trends in the mean percentage deviation data as the significant factors (EP, ET) were varied. These trend lines represent the effect of a single independent variable on the response disregarding the other process variable. According to **Fig. 7**. **a)** the exposure time slightly dominates against the exposure power for deviation of $d_{s,CAD}$=200 µm. The exposure power dominates against the exposure time for the mean of deviation of $d_{s,CAD}$=300 µm, $d_{s,CAD}$=400 µm and $d_{s,CAD}$=500 µm (**Fig. 7**. **b), c)** and **d)**). The lowest point on the graph indicates the factor level that has a minimum deviation in the response. Clearly, for each condition, different values of factors and levels will yield the least mean of deviation. A similar analysis was performed to interpret the effect of the interactions, where the impact of one factor depends on the level of the other factor. From **Fig. 8** it can be observed that the least deviation for $d_{s,CAD}$=200 µm and $d_{s,CAD}$=300 µm is achieved with the mid-level of EP when ET is at the highest level for $d_{s,CAD}$=200 µm (**Fig. 8. a)**) and at the lowest level for $d_{s,CAD}$=300 µm (**Fig. 8. b)**). When EP is at mid-level, lower deviations are seen for $d_{s,CAD}$=400 µm and $d_{s,CAD}$=500 µm at the lowest level of ET. Nonetheless, the least deviation is achieved when EP is at the lowest level and ET at the highest level for d_{sCAD}=400 µm and mid-level for d_{sCAD}=500 µm. Based on **Fig. 8**, in order to generate a minimum percentage deviation (i.e. maximum printing accuracy), the following process parameters can be considered: EP= 14 mW/cm^2, ET=3 s for $d_{s,CAD}$=200 µm, EP= 14 mW/cm^2, ET=1.5 s for $d_{s,CAD}$=300 µm, EP=6.72 mW/cm^2, ET=3 s for $d_{s,CAD}$=400 µm, EP=6.72 mW/cm^2, ET=2 s for $d_{s,CAD}$=500 µm.

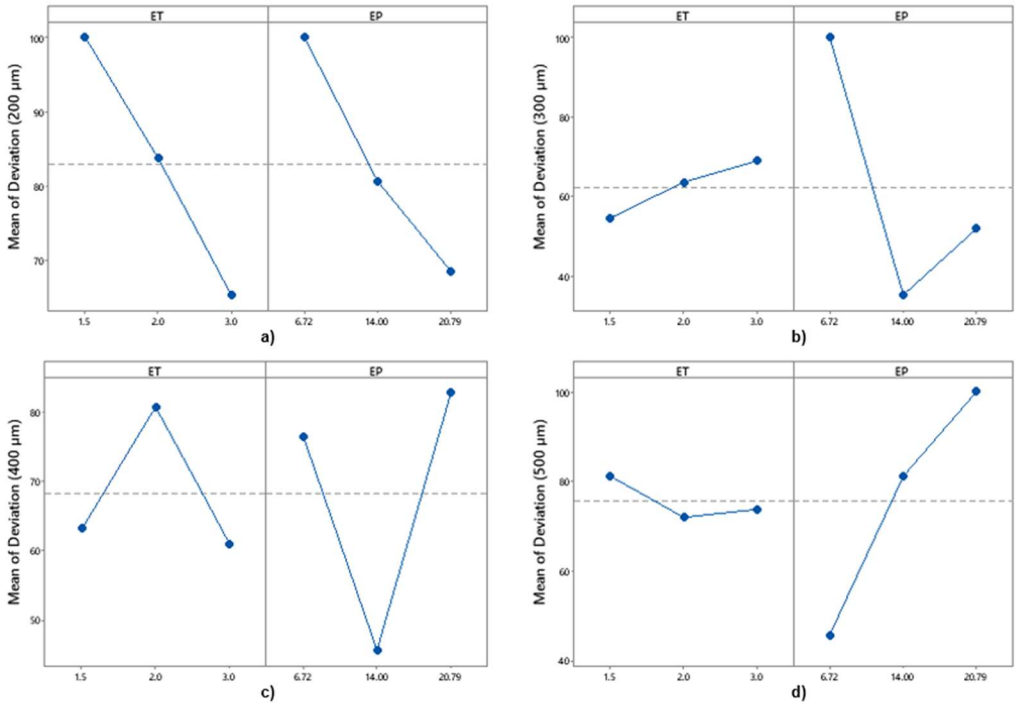

Fig. 7. Effect of the significant process parameters on the mean of deviation for a) $d_{s,CAD}$=200 µm b) $d_{s,CAD}$=300 µm c) $d_{s,CAD}$=400 µm d) $d_{s,CAD}$=500 µm

Generally, to ensure the adhesion between the layers, the cure depth needs to be a couple of times higher than the applied layer thickness [19, 47, 48]. The initial layers of the sliced CAD model with $d_{s,CAD}$=100 µm are essentially circles with a diameter of 100 µm and an area of 7853 µm^2. Due to this particularly small exposed area, the attaching force between the layer and the transparent foil is higher than the bonding force

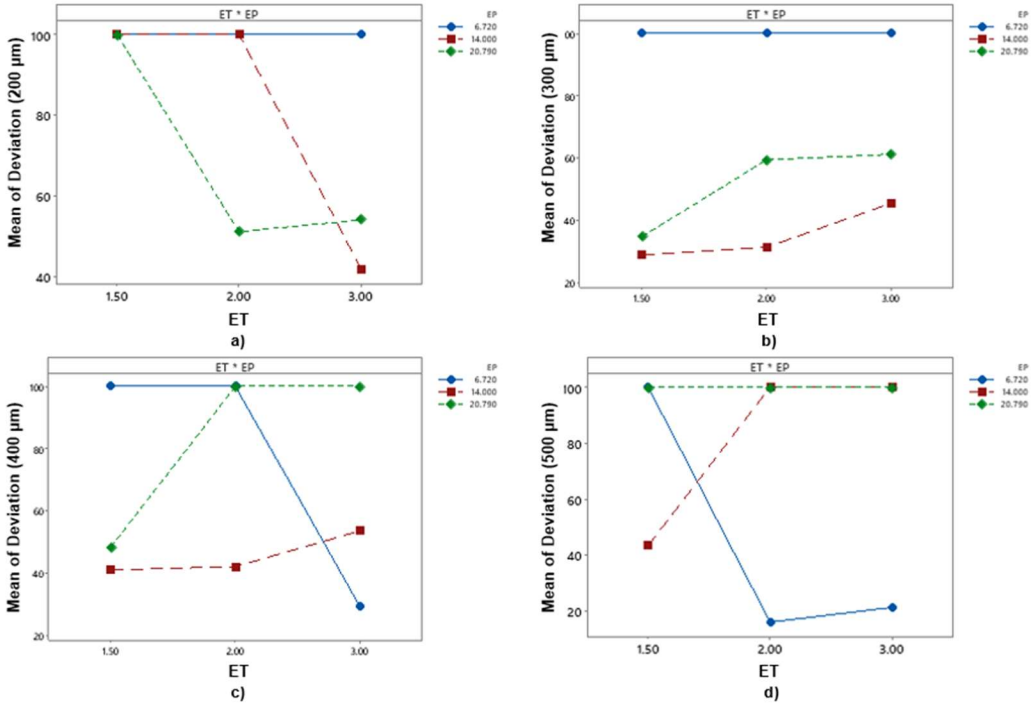

Fig. 8. Significant interaction effects for a) $d_{s,CAD}$=200 µm b) $d_{s,CAD}$=300 µm c) $d_{s,CAD}$=400 µm d) $d_{s,CAD}$=500 µm

of the layer with the previous layer. It is important to mention that the resulting energy density is well above the critical value for the exposure power of 6.72 mW/cm^2 and the exposure time of 1.5 s. Therefore, even though in theory the resolution may allow a construction of parts with resolution as low as 40 µm, the part with $d_{s,\,CAD}$=100 µm is not strong enough to withstand the manufacturing process. Similarly, findings in the literature indicate that the walls with CAD thickness less than 300 µm could not be manufactured via DLP process, and the thinnest stable walls had the thickness of 300 µm to 400 µm [19]. This suggests that to ensure adequate adhesion between the adjacent layers, the cure depth must be significantly higher than the recommended cure depth. At the lowest exposure power (6.72 mW/cm^2) the only manufacturable lattices were those with designed strut diameter $d_{s,CAD}$=400 µm and 500 µm. **Fig. 9**. shows the printed sample of $d_{s,CAD}$=500 µm (left). This implies that the applied exposure energies and resulting cure depths were not sufficient for manufacturing of $d_{s,CAD}$ <400 µm. The minimum cure depth necessary to manufacture the CAD strut diameter of 500 µm at 6.72 mW/cm^2 was 143 µm, yielding the factor of 14.3 for the layer thickness of 10 µm and 5.72 for the layer thickness of 25 µm. For CAD strut diameter of 400 µm, the minimum cure depth necessary to manufacture at the power of 6.72 mW/cm^2 is 192 µm, yielding the factor of 19.2 for the layer thickness of 10 µm and 7.68 for the layer thickness of 25 µm. An increase of the exposure power to 14 mW/cm^2 resulted in the manufacturing of CAD strut diameters of 300 µm and 400 µm at all exposure times but distorted the 500 µm resulting in a fully solidified green part at higher exposure times (**Fig. 9. b)**). At the exposure power 14 mW/cm^2 and at both layer thicknesses the 500 µm sample was

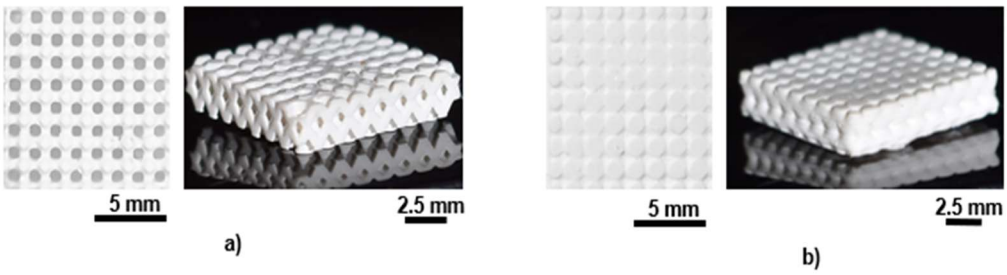

Fig. 9. a) Cross-section and side view of the green part $d_{s,CAD}$=500 µm (LT=25 µm, EP=6.72 mW/cm^2 , ET=2 s) and b) Cross-section and side view of the overexposed part $d_{s,CAD}$=500 µm (LT=25 µm, EP= 20.79 mW/cm^2, ET=2 s)

possible to manufacture at the lowest exposure time resulting in the cure depth of 196 µm yielding the factor of 19.6 for the layer thickness of 10 µm and 7.84 for the layer thickness of 25 µm. The 300 µm samples and 400 µm sample were manufacturable at all combinations of the exposure time, the exposure power and the layer thickness at cure depths of 196 µm, 231 µm, 280 µm. Furthermore, at the highest exposure time (3 s) the lattice structure with CAD strut diameter of 200 µm was possible to manufacture with cure depth of 280 µm, yielding the factor of 28 for the layer thickness of 10 µm and 11.2 for the layer thickness of 25 µm. The highest exposure power (20.79 mW/cm^2) resulted in completely dense $d_{s,CAD}$=500 µm sample, at both layer thicknesses. The samples with 400 µm CAD strut diameter were manufacturable at the lowest exposure time (1.5 s). Higher exposure times were necessary to manufacture the $d_{s,CAD}$=300 µm and $d_{s,CAD}$=200 µm and the minimum cure depth necessary for manufacturing was 196 µm and 280 µm, respectively. Comparing the $d_{s,CAD}$=500 µm and $d_{s,CAD}$=200 µm as the highest and lowest manufacturable samples, the $d_{s,CAD}$=200 µm requires almost double the cure depth than the $d_{s,CAD}$=500 µm. As the exposure

area increases, the necessary cure depth for the part to withstand the manufacturing process decreases. This leads to conclude that, for small exposure areas, higher cure depths are necessary for proper adherence of the adjacent layers. Although the recommended cure depths should be a couple of times higher than the layer thickness to avoid overcuring, the results suggest that the manufacturability of lattice structures is a factor of not only the cure depth, but also the size of the sliced layer exposure area and the overcuring effects should be considered when designing the starting CAD model.

3.3. Broadening behaviour

To evaluate the overgrowth in the horizontal direction, the cure excess width was plotted against the logarithm of the energy dose in **Fig. 10**. for $d_{s,CAD}$= 300 µm and $d_{s,CAD}$= 400 µm at two different layer thicknesses (LT= 10 and 25 µm), constant exposure power (14.79 mW/cm^2) and varying exposure time (1.5 s-3 s). Not enough data is present for samples with CAD strut diameter of 200 µm and 500 µm. Therefore, only the excess cure widths for 300 µm and 400 µm were plotted. Gentry and Halloran [30] reported a linear relationship of the cure width and logarithm of the energy dose. Contrarily, Rudraraju [36] reported that the cure width varies linearly with respect to the energy dose [30, 36]. The relationship between the cure width and the logarithm of the energy dose from our experimental results based on 3D samples is linear following the quasi-Beer Lambert model, similar to work reported by Gentry and Halloran [30]. Since the Equation 2 is derived from Jacob's equation for the working curve of the slurry, it is assumed that the E_w and D_w are constants and solely characteristics of the slurry [36]. However, for broadening

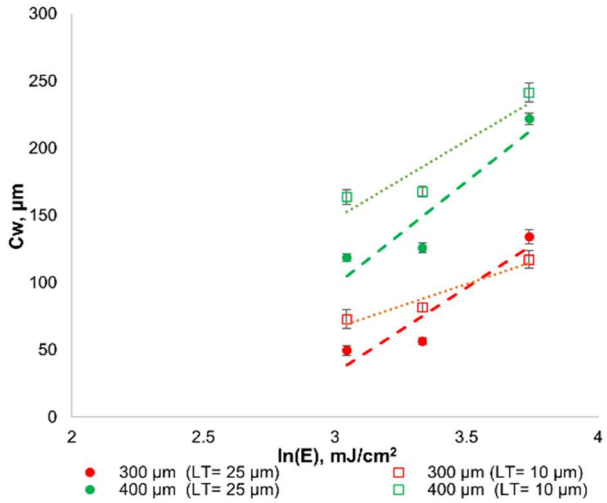

Fig. 10. Variation of cure width (C_w) with respect to the logarithm of the energy dose

phenomena this is not the case. **Table 6** contains a summary of the constants E_w and D_w for different layer thicknesses and feature sizes. Depth at the onset of broadening, B_d (Equation 3) was calculated to describe the effect of broadening in the suspension [30].

For $d_{s,CAD}$= 300 µm E_w and D_w are lower with respect to $d_{s,CAD}$= 400 µm for both layer thicknesses. With the increase of the layer thickness, the parameters E_w and D_w increase for both $d_{s,CAD}$= 300 µm and $d_{s,CAD}$= 400 µm. It is evident that E_w decreases with the increase of the feature size, whereas D_w increases with the increase of the feature size, in accordance with the literature [36]. Moreover, the broadening increases with

Table 6 Critical width energies and width sensitivities

	LT= 10 µm			LT= 25 µm		
$d_{s,CAD}$, µm	E_w, mJ/cm^2	D_w, µm	Bd, µm	E_w, mJ/cm^2	D_w, µm	Bd, µm
300	6.69	65.43	-36.29	15.64	126.42	66.34
400	5.47	116.52	-60.44	10.48	154.73	18.04

the energy dose. To limit the excess broadening, lower width sensitivity is desired [30]. Similar trends of broadening behaviour were reported in the literature, where it was found that the broadening depends upon the feature size and the energy dose for a single-layer curing [30, 36, 39]. Here, we report that layer thickness has an influence on the broadening parameters. This is the consequence of the decrease of side scattering with the increase of layer thickness where the light propagates more into the vertical direction before it gets scattered to the horizontal direction. Furthermore, B_d is negative for the layer thickness of 10 µm. This is seemingly contrary to practicality, as negative cure depths are not realistic. However, it indicates that at LT= 10 µm for all energy doses (in the experimental range) the broadening will occur at all cure depths. At LT= 25 µm the broadening will start to occur at cure depths of 66.34 µm and higher for $d_{s,CAD}$= 300 µm and 18.04 µm and higher for $d_{s,CAD}$= 300 µm. The results show that the broadening is inevitable with the current ceramic slurry composition.

The experimental strut dimensions are all found to have a large deviation from the designed values. The larger experimental strut dimensions can be attributed to the following reasons. Firstly, the addition of the ceramic particles into the resin attributes to the scattering of light within the suspension. The scattering phenomena is usually attributed to the difference in the refractive indices of the resin and ceramic particles [39, 49]. The blank resin had a RI of 1.49 whereas the alumina powder has RI of 1.77 yielding the RI contrast of 0.28 [50]. The scattering effects could be reduced by modifying the UV curable resin's refractive index [51]. Secondly, the control of the dimensional overgrowth could be achieved by the addition of UV blockers or absorbers, which could, on the other hand, lead to unfavourable cure depth reduction [42, 52]. Furthermore, as high cure depths were necessary for successful manufacturing, the lateral overcuring had the effect of the deviation from the CAD models. For the part with the smallest strut diameter ($d_{s,CAD}$=200 µm), the cure depth necessary was almost double than that of the sample with $d_{s,CAD}$=500 µm. This implies that with the increase of the exposed area, the energy dose and consequently the cure depth should be lower to reach the least deviation. Lastly, the control of the part's dimension could be achieved by using a correction factor to modify the starting CAD model. To manufacture a lattice structure with precisely dimensioned features for a particular application it is vital to select the optimal processing conditions or to account for the geometrical overgrowth of the strut diameters relative to the design diameter.

4. Conclusions

In the present study, two preparation methods of Al_2O_3 photopolymerizable slurries for DLP were described. There was a need to control the process parameters and materials for the lattice structures fabrication. The main factors that influence the printing accuracy were investigated. Full factorial design

of experiments was used to assess the influence of the exposure power, the exposure time and the layer thickness accordingly.

The conclusions drawn from the study are as follows:

- The slurry prepared with the pre-treated powder exhibited Non-Newtonian behaviour with acceptable viscosity for successful processing on the Admaflex 130.
- The depth of penetration, which is crucial for dimensional accuracy, was lower for the ceramic slurry with the pre-treated powder.
- Lattices with strut diameter of 100 μm were not strong enough to withstand the manufacturing process. However, lattices with CAD designed struts of 200-500 μm were successfully manufactured. The cure depth necessary for successful manufacturing was found to be inversely proportional to the exposed area.
- The experimental strut diameters were found to be larger than the designed values for all manufactured samples. This is attributed to the light scattering within the ceramic slurry due to the refractive index contrast between the ceramic powder and the resin and the overcuring effect necessary for a successful build.
- According to the DOE, the most significant parameters that directly influence the dimensional accuracy were the exposure time, the exposure power and the interaction of both.
- The excess cure width was found to linearly increase with the logarithm of the energy dose.
- The broadening parameters were found to be dependent on the layer thickness as well as the energy dose and the feature size.

By careful control of the process parameters and by using appropriate preparation of the photopolymerizable slurry, the dimensional accuracy of the lattice structures can be improved. Further research of the broadening behaviour should be conducted to gain a better understanding of the lateral accuracy in DLP technology. Different orientation and position of the model on the building plate could possibly have an influence the dimensional accuracy. The investigation of different formulations of the resin is necessary to understand how different components influence the broadening behaviour of a 3D printed sample. Nevertheless, the findings from this work can serve as a guideline for photopolymerizable slurry preparation and for adjusting the printing parameters to improve the dimensional characteristics of 3D printed ceramic lattices.

Acknowledgements

The research leading to these results has received funding from the Engineering and Physical Sciences Research Council for project FACE - Novel Integrated Fuel Reformer-Aftertreatment System for Clean and Efficient Road Vehicles under grant number EP/P031226/1. N.K. also thanks the University of Birmingham for award of a PhD scholarship.

References

1. Lin K, Sheikh R, Romanazzo S, Roohani I (2019) 3D printing of bioceramic scaffolds-barriers to

the clinical translation: From promise to reality, and future perspectives. Materials (Basel) 12: . https://doi.org/10.3390/ma12172660

2. Papetti V, Dimopoulos Eggenschwiler P, Della Torre A, Lucci F, Ortona A, Montenegro G (2018) Additive Manufactured open cell polyhedral structures as substrates for automotive catalysts. Int J Heat Mass Transf 126:1035–1047 . https://doi.org/10.1016/j.ijheatmasstransfer.2018.06.061

3. Flores I, Kretzschmar N, Azman AH, Chekurov S, Pedersen DB, Chaudhuri A (2020) Implications of lattice structures on economics and productivity of metal powder bed fusion. Addit Manuf 31:100947 . https://doi.org/10.1016/j.addma.2019.100947

4. Elsayed M, Ghazy M, Youssef Y, Essa K (2019) Optimization of SLM process parameters for Ti6Al4V medical implants. Rapid Prototyp J 25:433–447 . https://doi.org/10.1108/RPJ-05-2018-0112

5. Hassanin H, El-Sayed MA, Elshaer A, Essa K, Jiang K (2018) Microfabrication of net shape zirconia/alumina nanocomposite micro parts. Nanomaterials 8: . https://doi.org/10.3390/nano8080593

6. Sabouri A, Yetisen AK, Sadigzade R, Hassanin H, Essa K, Butt H (2017) Three-Dimensional Microstructured Lattices for Oil Sensing. Energy and Fuels 31:2524–2529 . https://doi.org/10.1021/acs.energyfuels.6b02850

7. Sun C, Zhang X (2002) The influences of the material properties on ceramic micro-stereolithography. Sensors Actuators, A Phys 101:364–370 . https://doi.org/10.1016/S0924-4247(02)00264-9

8. Kovacev N, Li S, Zeraati-Rezaei S, Hemida H, Tsolakis A, Essa K (2020) Effects of the internal structures of monolith ceramic substrates on thermal and hydraulic properties: additive manufacturing, numerical modelling and experimental testing. Int J Adv Manuf Technol. https://doi.org/10.1007/s00170-020-06493-2

9. Bikas H, Stavropoulos P, Chryssolouris G (2016) Additive manufacturing methods and modeling approaches: A critical review. Int J Adv Manuf Technol 83:389–405 . https://doi.org/10.1007/s00170-015-7576-2

10. Yang L, Miyanaji H (2020) Ceramic additive manufacturing: A review of current status and challenges. Solid Free Fabr 2017 Proc 28th Annu Int Solid Free Fabr Symp - An Addit Manuf Conf SFF 2017 652–679

11. Zocca A, Colombo P, Gomes CM, Günster J (2015) Additive manufacturing of ceramics: Issues, potentialities, and opportunities. J Am Ceram Soc 98:1983–2001 . https://doi.org/10.1111/jace.13700

12. Jasveer S, Jianbin X (2018) Comparison of Different Types of 3D Printing Technologies. Int J Sci Res Publ 8:1–9 . https://doi.org/10.29322/ijsrp.8.4.2018.p7602

13. Farzadi A, Solati-Hashjin M, Asadi-Eydivand M, Osman NAA (2014) Effect of layer thickness and printing orientation on mechanical properties and dimensional accuracy of 3D printed porous samples for bone tissue engineering. PLoS One 9:1–14 . https://doi.org/10.1371/journal.pone.0108252

14. Tan C, Li S, Essa K, Jamshidi P, Zhou K, Ma W, Attallah MM (2019) Laser Powder Bed Fusion of Ti-rich TiNi lattice structures: Process optimisation, geometrical integrity, and phase transformations. Int J Mach Tools Manuf 141:19–29 . https://doi.org/10.1016/j.ijmachtools.2019.04.002

15. Essa K, Hassanin H, Attallah MM, Adkins NJ, Musker AJ, Roberts GT, Tenev N, Smith M (2017) Development and testing of an additively manufactured monolithic catalyst bed for HTP thruster applications. Appl Catal A Gen 542:125–135 . https://doi.org/10.1016/j.apcata.2017.05.019

16. Sing SL, Wiria FE, Yeong WY (2018) Selective laser melting of lattice structures: A statistical approach to manufacturability and mechanical behavior. Robot Comput Integr Manuf 49:170–180 . https://doi.org/10.1016/j.rcim.2017.06.006

17. Qiu C, Yue S, Adkins NJE, Ward M, Hassanin H, Lee PD, Withers PJ, Attallah MM (2015) Influence of processing conditions on strut structure and compressive properties of cellular lattice structures fabricated by selective laser melting. Mater Sci Eng A 628:188–197 . https://doi.org/10.1016/j.msea.2015.01.031

18. Fu X, Zou B, Xing H, Li L, Li Y, Wang X (2019) Effect of printing strategies on forming accuracy and mechanical properties of ZrO2 parts fabricated by SLA technology. Ceram Int 45:17630–17637 . https://doi.org/10.1016/j.ceramint.2019.05.328

19. Conti L, Bienenstein D, Borlaf M, Graule T (2020) Effects of the layer height and exposure energy on the lateral resolution of zirconia parts printed by lithography-based additive manufacturing. Materials (Basel) 13: . https://doi.org/10.3390/ma13061317

20. Schwarzer E, Holtzhausen S, Scheithauer U, Ortmann C, Oberbach T, Moritz T, Michaelis A (2019) Process development for additive manufacturing of functionally graded alumina toughened zirconia components intended for medical implant application. J Eur Ceram Soc 39:522–530 . https://doi.org/10.1016/j.jeurceramsoc.2018.09.003

21. Schhauer U, Schwarzer E, Moritz T, Michaelis A (2018) Additive Manufacturing of Ceramic Heat Exchanger: Opportunities and Limits of the Lithography-Based Ceramic Manufacturing (LCM). J Mater Eng Perform 27:14–20 . https://doi.org/10.1007/s11665-017-2843-z

22. Ozog P, Blugan G, Kata D, Graule T (2019) Influence of the Printing Parameters on the Quality of Alumina Ceramics Shaped by UV-LCM Technology. J Ceram Sci Technol 10:1–10 . https://doi.org/10.4416/JCST2019-00023

23. Shuai X, Zeng Y, Li P, Chen J (2020) Fabrication of fine and complex lattice structure Al2O3 ceramic by digital light processing 3D printing technology. J Mater Sci 55:6771–6782 .

https://doi.org/10.1007/s10853-020-04503-y

24. Guo J, Zeng Y, Li P, Chen J (2019) Fine lattice structural titanium dioxide ceramic produced by DLP 3D printing. Ceram Int 45:23007–23012 . https://doi.org/10.1016/j.ceramint.2019.07.346

25. Griffith ML, Halloran J (1994) Ultraviolet Curing of Highly Loaded Ceramic Suspensions for Stereolithography of Ceramics. Solid Free Fabr Symp 396–403

26. Johansson E, Lidström O, Johansson J, Lyckfeldt O, Adolfsson E (2017) Influence of resin composition on the defect formation in alumina manufactured by stereolithography. Materials (Basel) 10: . https://doi.org/10.3390/ma10020138

27. Peñaloza GAL (2018) Additive manufacturing of Zirconia. 71

28. Song SY, Park MS, Lee D, Lee JW, Yun JS (2019) Optimization and characterization of high-viscosity ZrO2 ceramic nanocomposite resins for supportless stereolithography. Mater Des 180:107960 . https://doi.org/10.1016/j.matdes.2019.107960

29. Hwa LC, Rajoo S, Noor AM, Ahmad N, Uday MB (2017) Recent advances in 3D printing of porous ceramics: A review. Curr Opin Solid State Mater Sci 21:323–347 . https://doi.org/10.1016/j.cossms.2017.08.002

30. Gentry SP, Halloran JW (2013) Depth and width of cured lines in photopolymerizable ceramic suspensions. J Eur Ceram Soc 33:1981–1988 . https://doi.org/10.1016/j.jeurceramsoc.2013.02.033

31. Hu K, Wei Y, Lu Z, Wan L, Li P (2018) Design of a Shaping System for Stereolithography with High Solid Loading Ceramic Suspensions. 3D Print Addit Manuf 5:311–318 . https://doi.org/10.1089/3dp.2017.0065

32. Komissarenko DA, Sokolov PS, Evstigneeva AD, Shmeleva IA, Dosovitsky AE (2018) Rheological and curing behavior of acrylate-based suspensions for the DLP 3D printing of complex zirconia parts. Materials (Basel) 11: . https://doi.org/10.3390/ma11122350

33. Griffith ML, Halloran JW (1997) Scattering of ultraviolet radiation in turbid suspensions. J Appl Phys 81:2538–2546 . https://doi.org/10.1063/1.364311

34. Abouliatim Y, Chartier T, Abelard P, Chaput C, Delage C (2009) Optical characterization of stereolithography alumina suspensions using the Kubelka-Munk model. J Eur Ceram Soc 29:919–924 . https://doi.org/10.1016/j.jeurceramsoc.2008.07.008

35. Bennett J (2017) Measuring UV curing parameters of commercial photopolymers used in additive manufacturing. Addit Manuf 18:203–212 . https://doi.org/10.1016/j.addma.2017.10.009

36. Rudraraju A V. (2013) Digital Data Processing and Computational Design for Large Area Maskless. Thesis 260

37. Varghese G, Moral M, Castro-García M, López-López JJ, Marín-Rueda JR, Yagüe-Alcaraz V, Hernández-Afonso L, Ruiz-Morales JC, Canales-Vázquez J (2018) Fabrication and

characterisation of ceramics via low-cost DLP 3D printing. Bol la Soc Esp Ceram y Vidr 57:9–18 . https://doi.org/10.1016/j.bsecv.2017.09.004

38. Sokolov PS, Komissarenko DA, Shmeleva IA, Slyusar I V., Dosovitskiy GA, Evdokimov P V., Putlyaev VI, Dosovitskiy AE (2018) Suspensions on the basis of stabilised zirconium oxide for three-dimensional printing. IOP Conf Ser Mater Sci Eng 347: . https://doi.org/10.1088/1757-899X/347/1/012012

39. Mitteramskogler G, Gmeiner R, Felzmann R, Gruber S, Hofstetter C, Stampfl J, Ebert J, Wachter W, Laubersheimer J (2014) Light curing strategies for lithography-based additive manufacturing of customized ceramics. Addit Manuf 1:110–118 . https://doi.org/10.1016/j.addma.2014.08.003

40. Zhang K, Xie C, Wang G, He R, Ding G, Wang M, Dai D, Fang D (2019) High solid loading, low viscosity photosensitive Al 2 O 3 slurry for stereolithography based additive manufacturing. Ceram Int 45:203–208 . https://doi.org/10.1016/j.ceramint.2018.09.152

41. Sun J, Binner J, Bai J (2019) Effect of surface treatment on the dispersion of nano zirconia particles in non-aqueous suspensions for stereolithography. J Eur Ceram Soc 39:1660–1667 . https://doi.org/10.1016/j.jeurceramsoc.2018.10.024

42. Wang JC, Dommati H (2018) Fabrication of zirconia ceramic parts by using solvent-based slurry stereolithography and sintering. Int J Adv Manuf Technol 98:1537–1546 . https://doi.org/10.1007/s00170-018-2349-3

43. Gonzalez P, Schwarzer E, Scheithauer U, Kooijmans N, Moritz T (2019) Additive manufacturing of functionally graded ceramic materials by stereolithography. J Vis Exp 2019:1–8 . https://doi.org/10.3791/57943

44. Tomeckova V, Halloran JW (2010) Predictive models for the photopolymerization of ceramic suspensions. J Eur Ceram Soc 30:2833–2840 . https://doi.org/10.1016/j.jeurceramsoc.2010.01.027

45. Delhote N, Bila S, Baillargeat D, Chartier T, Verdeyme S (2011) Advanced Design and Fabrication of Microwave Components Based on Shape Optimization and 3D Ceramic Stereolithography Process. Adv Ceram - Synth Charact Process Specif Appl. https://doi.org/10.5772/18322

46. Jang KJ, Kang JH, Fisher JG, Park SW (2019) Effect of the volume fraction of zirconia suspensions on the microstructure and physical properties of products produced by additive manufacturing. Dent Mater 35:e97–e106 . https://doi.org/10.1016/j.dental.2019.02.001

47. Borlaf M, Serra-Capdevila A, Colominas C, Graule T (2019) Development of UV-curable ZrO2 slurries for additive manufacturing (LCM-DLP) technology. J Eur Ceram Soc 39:3797–3803 . https://doi.org/10.1016/j.jeurceramsoc.2019.05.023

48. Zhang J, Wei L, Meng X, Yu F, Yang N, Liu S (2019) Digital light processing-stereolithography three-dimensional printing of yttria-stabilized zirconia. Ceram Int 0–1 . https://doi.org/10.1016/j.ceramint.2019.12.113

49. Sun C, Zhang X (2002) Experimental and numerical investigations on microstereolithography of ceramics. J Appl Phys 92:4796–4802 . https://doi.org/10.1063/1.1503410

50. Gentry SP, Halloran JW (2015) Light scattering in absorbing ceramic suspensions: Effect on the width and depth of photopolymerized features. J Eur Ceram Soc 35:1895–1904 . https://doi.org/10.1016/j.jeurceramsoc.2014.12.006

51. Badev A, Abouliatim Y, Chartier T, Lecamp L, Lebaudy P, Chaput C, Delage C (2011) Photopolymerization kinetics of a polyether acrylate in the presence of ceramic fillers used in stereolithography. J Photochem Photobiol A Chem 222:117–122 . https://doi.org/10.1016/j.jphotochem.2011.05.010

52. Wang J, Dommati H (2017) Applied Solvent-based slurry stereolithography process to fabricate high- performance ceramic earrings with exquisite details. Solid Free Fabr Symp 2790–2800